

Molecular Simulation of Carbon Dioxide Capture by Montmorillonite Using an Accurate and Flexible Force Field

Randall T. Cygan*

Geochemistry Department, Sandia National Laboratories, P. O. Box 5800, Albuquerque, New Mexico 87185-0754, United States

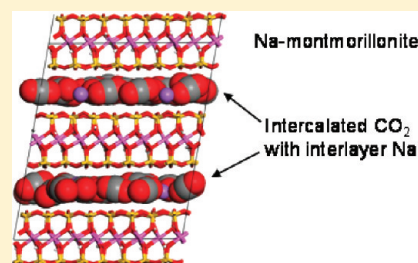
Vyacheslav N. Romanov

Geosciences Division, National Energy Technology Laboratory, P. O. Box 10940, Pittsburgh, Pennsylvania 15236, United States

Evgeniy M. Myshakin

National Energy Technology Laboratory, URS 626 Cochran Mill Road, Pittsburgh, Pennsylvania 15236, United States

ABSTRACT: Naturally occurring clay minerals provide a distinctive material for carbon capture and carbon dioxide sequestration. Swelling clay minerals, such as the smectite variety, possess an aluminosilicate structure that is controlled by low-charge layers that readily expand to accommodate water molecules and, potentially, CO₂. Recent experimental studies have demonstrated the efficacy of intercalating CO₂ in the interlayer of layered clays, but little is known about the molecular mechanisms of the process and the extent of carbon capture as a function of clay charge and structure. A series of molecular dynamics simulations and vibrational analyses have been completed to assess the molecular interactions associated with incorporation of CO₂ and H₂O in the interlayer of montmorillonite clay and to help validate the models with experimental observation. An accurate and fully flexible set of interatomic potentials for CO₂ is developed and combined with Clayff potentials to help evaluate the intercalation mechanism and examine the effect of molecular flexibility on the diffusion rate of CO₂ in water.



INTRODUCTION

Naturally occurring clay minerals provide a distinctive material for carbon capture and carbon dioxide sequestration. Recent experimental studies (Figure 1) have demonstrated that CO₂ adsorption (intercalation) capacity of clay mineral standards (from Clay Minerals Society) is comparable to that of coal.^{1–3} Abundance of swelling clays in U.S. regions of predominantly low-rank coal reserves provides an opportunity for their utilization as natural capture agents. In economic terms, clay minerals are a common natural resource and are literally dirt cheap. They are an attractive alternative to more complex materials that often require significant chemical functionalization to ensure acceptable carbon capture performance.^{4–6} Particularly attractive are swelling clay minerals, such as the smectite variety, which possess an aluminosilicate structure that is controlled by low-charge layers that easily expand to accommodate water molecules and, potentially, CO₂.

Clay-based materials could have a distinct advantage in that they can be used once and buried, saving the cost of regenerative energy, CO₂ compression, and subsurface injection. Sodium montmorillonite is a common clay mineral that has the potential for capture of CO₂ and provides a relatively stable environment for burial to help reduce carbon effects on the climate. The solubility of CO₂ within the interlayer of montmorillonite both at ambient conditions and at

elevated pressure–temperature conditions is unknown. It has been suggested that confinement of water modifies the dielectric constant of the water⁷ and can shift the acid constants of the confining surfaces and ultimately affect the solubility of CO₂. Experimental studies have been performed at the National Energy Technology Laboratory in Pittsburgh, PA to confirm the insertion and retention of CO₂ in the interlayer of montmorillonite.³ Stability of the CO₂–clay mineral composite will depend on the environmental conditions expected in the deep sequestration of supercritical CO₂ in sandstone and other sedimentary reservoirs, typically at temperatures greater than 305 K and pressures in the range of 15–50 MPa.^{8,9}

Infrared spectroscopy (FT-IR) has been used to monitor the conditions of insertion and the relative stability of various molecular species intercalated in clay interlayers.^{10–12} FT-IR studies have indicated that interlayer trapping of CO₂ can be irreversible,² which results in a distinct infrared absorption peak (Figure 2) corresponding to the asymmetric stretch vibration mode of the CO₂ molecule. This is supported by the hysteresis observed in adsorption–desorption plots (see Figure 1). Clay

Received: January 23, 2012

Revised: May 21, 2012

Published: May 25, 2012

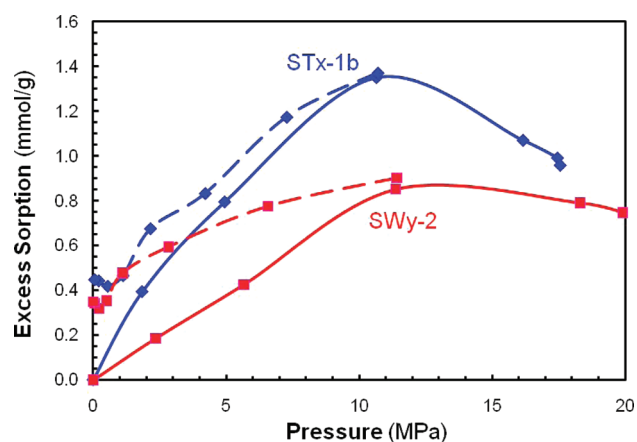


Figure 1. Insertion of CO₂ in smectite clay materials; Texas montmorillonite (STx) and Wyoming montmorillonite (SWy) samples exhibit limited adsorption at low pressures but swell at supercritical conditions as exhibited by the reduction in excess sorption above 10 MPa. Dashed lines represent desorption behavior.

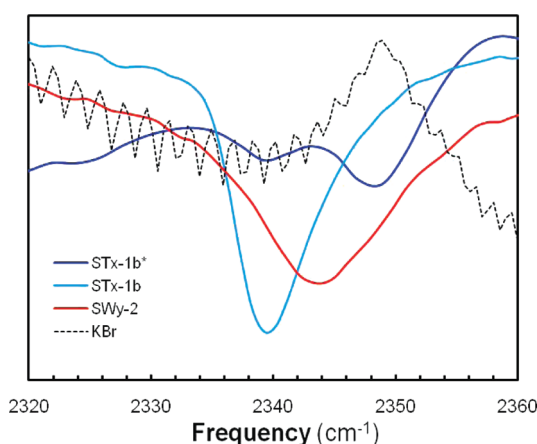


Figure 2. FT-IR diffuse-reflectance spectra of supercritical-CO₂-treated smectite clay powders, STx-1b and SWy-2 (KBr reflectance spectra was used for background subtraction); dark blue line represents transitional spectra after exposure of STx-1b to CO₂ gas.

mineral samples for these experiments were hermetically sealed in pressure vessels, exposed to vacuum conditions, and then treated with dry research-grade CO₂; water was absent from the pressure vessels. The interlayer of smectite clays also includes counterbalancing cations such as Na⁺ (dominant in SWy-2 montmorillonite) and Ca²⁺ (dominant in STx-1b) that balance the negative layer charge and have strong affinity to water. Residual water content can therefore be expected as a part of the first hydration shells of the interlayer ions. Experimental studies have demonstrated the efficacy of intercalating CO₂ in the interlayer of layered clays,¹³ but little is known about the molecular mechanisms of the process and the extent of carbon capture as a function of clay charge and structure. The exchangeable interlayer cations may significantly affect the CO₂ intercalation capacity of clay as well as the strength of the binding interactions within the interlayer that is reflected in the magnitude of the vibrational frequency shifts (see Figure 2). While the observed shifts were highly reproducible for each interlayer cation type after exposure to high-pressure supercritical CO₂, the lower-pressure experiments resulted in observation of transient peaks, including the one centered near the fundamental asymmetric stretch frequency (shown in Figure 2 for Ca–montmorillonite).

We have completed a series of molecular dynamics simulations to better assess the molecular interactions associated with incorporation of CO₂ in the interlayer of montmorillonite and to simulate vibrational spectra to help validate the models with experimental observation. To this purpose we have developed a flexible force field for CO₂ capable to describe interfacial behavior and be useful in spectroscopic analysis. This study follows the examples provided in previous efforts to link experimental vibrational analysis with large-scale molecular dynamics simulations of layered materials.^{14,15} The computational chemistry investigation provides a proof of concept that molecular simulation methods have the capability and accuracy to predict the mechanisms associated with CO₂ capture in complex natural materials.

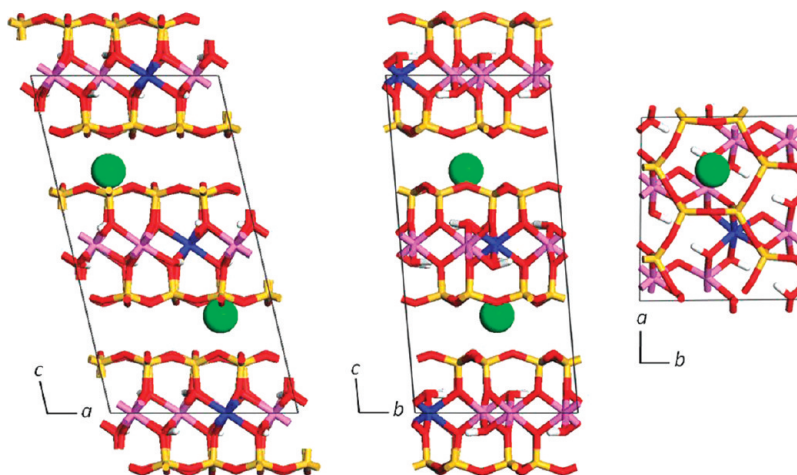


Figure 3. Structure of 2 × 1 × 2 Na–montmorillonite cell exhibiting two layers of the aluminosilicate lattice with O atoms (red) and H atoms (white); Mg atoms (blue) substitute for Al (pink) in the octahedral sheet; Si atoms (yellow) in the tetrahedral sheet; interlayer Na cations are represented as green spheres. No interlayer water is associated with the structural model.

MOLECULAR SIMULATIONS

Molecular Models of Montmorillonite. Sodium montmorillonite is a common soil phase that results from the weathering and alteration of basic rock types typically having low potassium contents under alkaline conditions. The normally nanosized platy material is characterized by planar sheets of silica tetrahedra and alumina octahedra that coordinate to form a TOT (tetrahedron–octahedron–tetrahedron) layer that is negatively charged by the aliovalent substitution of Mg^{2+} for Al^{3+} in the octahedral sheet (Figure 3). The negative charge is balanced by the incorporation of Na cations in the interlayer. Smectite clays, like montmorillonite, typically have a relatively low layer charge (c.f., muscovite) and therefore can be easily expanded by the insertion of water molecules into the interlayer to hydrate the Na^+ and internal surface of the tetrahedral sheet. The general chemical formula for sodium montmorillonite is given by $\text{Na}_x\text{Mg}_y\text{Al}_{2-x}\text{Si}_4\text{O}_{10}(\text{OH})_2 \cdot n\text{H}_2\text{O}$ where all of the layer charge resides on the octahedral sheet, although tetrahedral substitutions such as Al^{3+} for Si^{4+} can also occur to augment the net negative layer charge. Hydroxyl groups in TOT clays are associated with the octahedra sheet. Montmorillonite has hydroxyl groups that are affected by vacancies that occur for every two occupied Al octahedra (see Figure 3). Silica tetrahedra form a hexagonal ring structure (as viewed along the *c*-axis) that influences the disposition of interlayer species. Figure 3 shows interlayer Na^+ that binds at the hexagonal holes in the tetrahedral sheet, which in turn modifies the equilibrium position of the hydroxyl groups directly below the hole.

An expanded representation of sodium montmorillonite is presented in Figure 4 where the clay is based on the smaller

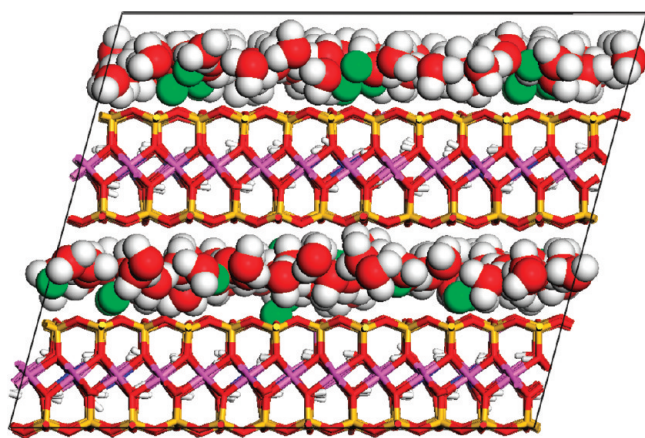


Figure 4. Snapshot of an equilibrated molecular dynamics simulation of sodium montmorillonite showing the Na^+ and water molecules in the interlayer; projection view is along the *b*-axis.

structure of Figure 3 with the addition of a single layer of water in the interlayer. The equilibrated structure is taken from a large-scale molecular dynamics simulation a $12 \times 4 \times 2$ supercell having 36 Na^+ and 192 water molecules in the interlayer. Details of the molecular dynamics simulations are discussed in a later section.

Because of the nanosized nature of clay materials and lack of suitable large single crystals for accurate structure determinations, molecular simulations have played a significant role in understanding clay structure and behavior. The swelling behavior of clay phases, in particular, has been examined to

better evaluate the energy and hydration state of clay minerals.^{14,16} Figure 5 presents the results of a series of molecular dynamics simulations using an isothermal–isobaric ensemble to evaluate the expansion of the clay with increasing water content. This example, from Cygan et al.,¹⁴ shows the expansion of montmorillonite (primarily octahedral charge) with the development of a hydrogen-bonded network of water molecules and the solvation of Na^+ to stabilize the interlayer and overcome the electrostatics that hold the layers together. Once expanded, the open interlayer region allows the backfill of water molecules to further stabilize the hydrogen-bonding network until critical water content is reached and the clay interlayer swells to accommodate two water layers. The fine structure of the swelling curve is in very good agreement with experimental findings.¹⁷ The simulations also suggest the possibility of forming a third water layer that becomes somewhat diffuse at the higher water content, but which is not observed in experiment.

Computational Methods. Classical Methods. Classical molecular dynamics (MD) was used to evaluate the structure and behavior of gaseous, liquid, and supercritical CO_2 , montmorillonite, and CO_2 -intercalated montmorillonite. Quantum chemistry methods, including those based on density functional theory, are theoretically more accurate but computationally expensive and cannot efficiently simulate the large number of atoms and time steps necessary to accurately model clay structures. We employ the Clayff force field¹⁴ that uses an empirically derived set of interaction parameters to accurately describe the potential energy between atoms in the clay structure. Clayff has been used extensively to successfully simulate many oxide, hydroxide, and hydrated systems including bulk and interfacial structures.^{14,18,19} The Forcite software²⁰ and Clayff parameters were used to evaluate the electrostatic and short-range interactions for each atomic configuration and time step.

Unfortunately, empirical force fields for the accurate simulation of CO_2 systems have not been fully developed, especially for interactions with oxide and silicate materials. Three-site models for CO_2 that are most compatible with Clayff have been examined,^{21,22} but the models lack bond flexibility and are incapable of providing an accurate description of the vibrational behavior of gaseous and condensed CO_2 liquids. A fully flexible model is required in order to evaluate the vibrational state of CO_2 within the clay interlayer, especially if vibrational spectroscopy is to provide an accurate diagnostic tool for CO_2 intercalation. Details of the force field development are provided in a later section.

Molecular dynamics simulations were performed using either a canonical *NVT* ensemble maintaining a fixed cell volume for a fixed number of atoms or an isothermal–isobaric *NPT* ensemble where the simulation cell can freely expand or contract. All simulation cells have *P1* symmetry where all atoms are allowed to freely translate throughout the entire simulation. Temperature was controlled using the Nosé–Hoover²³ method, and the Berendsen et al.²⁴ algorithm was used for controlling pressure of the simulation cell. One million time steps of 1 fs were used for most of CO_2 simulations to obtain a total of 1 ns of simulation time; atomic configurations were saved every 1000 time steps (1 ps) for efficient data storage and trajectory analysis. MD simulations were performed at various temperatures and pressures for evaluating subcritical CO_2 , and at 310 K (constant volume) or 310 K and 20 MPa for the *NPT* ensemble for supercritical CO_2 simulations. MD simulations for

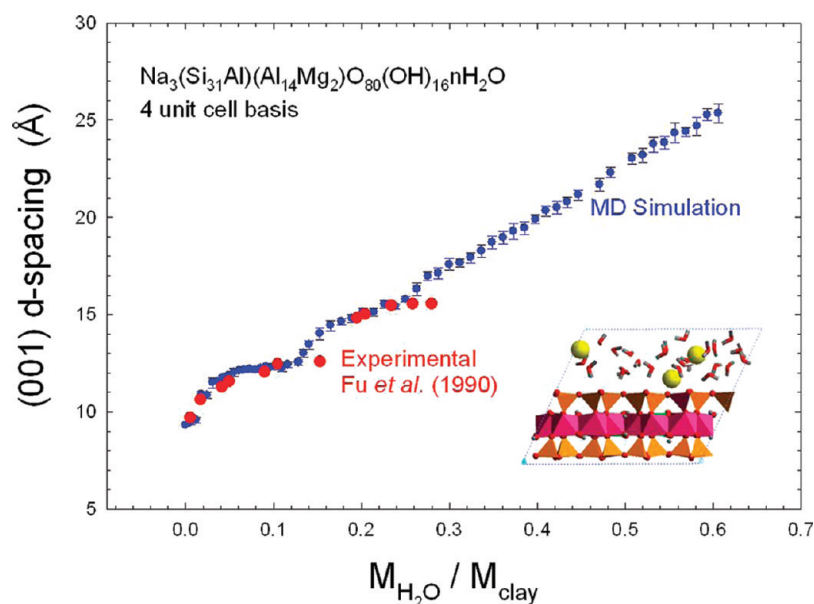


Figure 5. Swelling behavior of a montmorillonite clay based on *NPT* molecular dynamics simulations equilibrated at 300 K and 0.1 MPa.

montmorillonite and CO_2 –montmorillonite systems were completed at 300 K and 0.1 MPa (surface conditions) or 310 K and 20 MPa (supercritical CO_2 conditions), using 1 fs time steps for 1 ns of total simulation time. Once equilibrated, an additional 40 ps of simulation was performed for each system saving atomic positions and velocities for power spectra determinations. Simulations of gas phase CO_2 used periodic cells including 176–1408 molecules, whereas calculations of liquid and supercritical CO_2 used 512 molecules. Clay– CO_2 simulations involved a $6 \times 4 \times 2$ supercell of montmorillonite having 40 CO_2 molecules corresponding to a density equivalent to that of liquid CO_2 . Initially, no water was incorporated with the CO_2 in the montmorillonite interlayer; however, a series of nine additional MD simulations (*NPT* ensemble at 310 K and 20 MPa) were performed to address the influence of water on CO_2 intercalation. Carbon dioxide (two CO_2 molecules per unit cell) was added to hydrated montmorillonite to achieve CO_2 mole fractions ranging from 0.18 to 0.67 for the interlayer fluid. Power spectra were derived for two of the equilibrated simulations. Radial distribution functions describing H_2O – CO_2 structure within the interlayer were derived from atomic trajectories from a similar series of MD simulations (*NPT* ensemble at 348 K and 15 MPa) for a comparison of interatomic potentials. A recent molecular simulation study²⁵ has used Monte Carlo methods to examine the interlayer structure of Na–montmorillonite for H_2O – CO_2 mixtures but at lower CO_2 contents.

Power spectra are derived from the stored atomic velocities by evaluating the velocity autocorrelation function (VACF) and the Fourier-transformed power spectra.²⁶ For power spectra calculations, the atomic velocities were collected every 4 fs over a simulation time of 40 ps. Sampling every 4 fs ensured that the vibrational modes up to 4166 cm^{-1} were captured. A windowing gap of 1500 frames (6 ps) was used to give a resolution of approximately 2.8 cm^{-1} . The resulting power spectra represent the coordinated motions of atoms that correlate to bond stretches, bond angle bends, librations, intermolecular motions, and translations. Typically, the power spectrum modes are equivalent to the vibrational bands

associated with infrared and Raman spectra but without the limitations of selection rules.

Additional MD simulations were performed to examine the diffusion rate of CO_2 in aqueous solution. Cubic simulation cells consisting of 1720 water and 8 CO_2 molecules were examined using an *NVT* ensemble at several temperatures from 293 to 368 K, based on 0.1 MPa densities. The limited solubility of CO_2 in water suggests approximately 0.5–1 CO_2 for such a cell. However, to improve statistics, the number of CO_2 molecules was increased to eight assuming no interaction between CO_2 molecules during simulations. MD simulation times of 4 ns were completed. Atomic trajectories and mean square displacements were used to derive diffusion coefficients. To estimate CO_2 diffusion coefficients, the Einstein relation was employed using the equilibrated atomic trajectories, with 1 ps sampling, to evaluate the mean square displacement of CO_2 molecules.

$$D = \lim_{t \rightarrow \infty} \frac{1}{6N_m t} \left\langle \sum_{j=1}^{N_m} [r_j(t) - r_j(0)]^2 \right\rangle \quad (1)$$

Simulation time was 4 ns for each temperature. Diffusion coefficients were derived from the linear slope of mean square displacement as a function of simulation time; different restart points in the analysis were taken to monitor convergence.

Quantum Methods. High-level electronic structure calculations and normal-mode analysis were performed for cluster models of CO_2 and Na^+ – CO_2 . The Gaussian 03 software²⁷ was used to examine the clusters at two levels of theory. A hybrid functional B3LYP was implemented that combines the Becke²⁸ hybrid functional for Hartree–Fock exchange and DFT correlation with the local correlation of Vosko et al.²⁹ and the nonlocal correlation of Lee et al.³⁰ The Møller–Plesset³¹ correction for the correlation energy in a Hartree–Fock calculation, truncated at the second order (MP2), was used to investigate the two cluster models.^{32,33} Aug-cc-pVDZ basis set was used for each of the two methods. Vibrational analysis of the optimized structures was then performed to derive the normal modes of the clusters.³⁴

RESULTS AND DISCUSSION

Classical Simulations. Development of CO₂ Force Field.

A general review of the computational chemistry literature determined that energy force fields for the classical simulation of CO₂ systems were limited, especially for a force field based on a three-site model of CO₂. Our primary goal for the project was to use a simple three-site model that could easily be coupled with similar preexisting force fields that accurately model water, aqueous solutions, and mineral systems. Furthermore, we desired a fully flexible force field that would allow the direct coupling of energy and momentum between liquids and solids for improved accuracy in interfacial simulations. Improved models of surface structures, transport rates, electrostatics, electric double layers, and other critical phenomena require full relaxation of the molecular system without any atomic constraints such as keeping part of the system rigid. It is also important for molecules like H₂O and CO₂ to include bond stretch and bond bend terms in the force field to provide vibrational data, help to characterize interfacial behavior, and support experimental and spectroscopic analyses. Interatomic potentials for H₂O that incorporate bond flexibility are relatively common and have demonstrated improved predictions of thermodynamic properties across a wide range of state points compared to rigid models, particularly in the supercritical regime.³⁵

Rigid models for CO₂ have been successfully developed to accurately model the structure and thermodynamics of gas, liquid, and supercritical CO₂.^{21,36–38} The Harris and Young²¹ potential model, in particular, is very successful in reproducing the vapor–liquid coexistence curve for CO₂ and has been modified to include a flexible bond angle. The van der Waals potential and the point charges were optimized to reproduce the correct pressures, internal energies, and quadrupole moment. However, the force constant for the bond angle term was not fully developed and fails to predict the experimental deformation mode for vibration of the molecule. Nieto-Draghi et al.³⁶ used quantum mechanical calculations to evaluate bond stretch energies and a force constant for determination of thermal conductivity and shear viscosity of CO₂ but did not evaluate vibrational behavior. Qin et al.²² used the Harris and Young²¹ potential, adding a bond stretch term, to evaluate supercritical CO₂ and its interactions on silica surfaces. However, no critical examination was made on the choice of force constants and their effect on vibrational spectra or interfacial structure. Nonetheless, it is clear that the incorporation of flexibility is a significant contribution toward improving the accuracy of modeling CO₂ systems, especially for those involving interfaces where energy and momentum transfer strongly affects local structure and dynamics. Simulations of interfaces between liquid or supercritical CO₂ and an aqueous phase, or those between CO₂ and a solid, such as the sequestration of CO₂ in the interlayer of a clay mineral, will necessarily require refinements in interatomic potentials to accurately describe the molecular structure and behavior.

In our molecular simulations, we expand the previous three-site potentials for CO₂ and develop a fully flexible model, allowing for intramolecular bond stretch and angle bend. Equation 2 provides the general expression of the total potential energy in terms of the contributing terms.

$$E_{\text{Total}} = E_{\text{Coul}} + E_{\text{VDW}} + E_{\text{Stretch}} + E_{\text{Bend}} \quad (2)$$

Coulombic and van der Waals contributions represent the nonbonded energies, and the stretch and bend terms represent the intramolecular energies. The Coulombic or electrostatics energy is given by eq 3 where q_i and q_j are the partial charges of the atoms and r_{ij} is the distance between the atoms.

$$E_{\text{Coul}} = \frac{q_i q_j}{r_{ij}} \quad (3)$$

We assume electrostatics interactions occur in vacuum and that no dielectric medium is present to limit the interaction. A conversion factor is used to maintain appropriate energy units (kJ/mol) for this equation. The short-range van der Waals energy is given by

$$E_{\text{VDW}} = 4\varepsilon_{ij} \left[\left(\frac{\sigma_{ij}}{r_{ij}} \right)^{12} - \left(\frac{\sigma_{ij}}{r_{ij}} \right)^6 \right] \quad (4)$$

where ε_{ij} and σ_{ij} are optimized for intermolecular interactions. Standard Lorentz–Bertholet mixing rules are used to evaluate heteroatomic interactions for this expression.³⁹ Harmonic potentials are used for the bond stretch and angle bend terms:

$$E_{\text{Stretch}} = \frac{1}{2} k_s (r_{ij} - r_o)^2 \quad (5)$$

$$E_{\text{Bend}} = \frac{1}{2} k_B (\theta_{ijk} - \theta_o)^2 \quad (6)$$

Both energy expressions increase the potential energy using force constants k_s and k_B and deviations from the equilibrium geometry (r_o and θ_o). The total potential energy for any configuration of CO₂ molecules in a periodic simulation cell is evaluated using this set of potentials by summing all possible pairwise interactions. Ewald summation is used to ensure convergence of the long-range Coulombic energy (eq 3). The Coulombic and van der Waals contributions are excluded when evaluating intramolecular interactions.

Our refinement of force field parameters was obtained by combining the expanded potentials of Zhu et al.⁴⁰ based on the original parameters of Harris and Yung.²¹ We initially incorporated the force constants of Qin et al.²² and Liang and Lipscomb⁴¹ but were disappointed in their poor performance in simulating vibrational spectra for CO₂ phases. Ultimately, we optimized the stretch and bend force constants through a series of molecular dynamics simulations and power spectra calculations. The force constant for the CO₂ bend was determined by directly matching the observed frequency of 667 cm⁻¹.⁴² The force constant for the bond stretch is more problematic due to the occurrence of symmetrical and asymmetrical modes, observed, respectively, at 1330 and 2349 cm⁻¹;^{42,43} the symmetrical stretch mode is infrared inactive due to the lack of a net dipole during the vibrational motion. Because of the coupling of the two stretch modes through a single force constant, it was necessary to minimize the mismatch for the peaks while placing more weight on the asymmetric stretch that dominates the intensity in theoretical spectra. We incorporated the identical equilibrium bond distance and bend angle used by Zhu et al.⁴⁰ for the intramolecular potentials for CO₂. The bend and asymmetrical peaks are in agreement with experiment to within 3 cm⁻¹, however, the frequency for the symmetrical stretch is underpredicted by approximately 100 cm⁻¹. The nature of the potentials for the simple three-site model limits the

decoupling of the stretch models and improving the accuracy of the symmetrical stretch frequency.

The optimized force field parameters for CO₂ are presented in Table 1. The parameters were used for the bulk CO₂

Table 1. Force Field Parameters for CO₂

Nonbond		
q_C		+0.6512 e
q_O		−0.3256 e
ϵ_C		0.2340 kJ/mol
ϵ_O		0.6683 kJ/mol
σ_C		2.800 Å
σ_O		3.028 Å
Bond		
k_{CO}		8443 kJ/mol Å ²
$r_{o\ CO}$		1.162 Å
k_{OCO}		451.9 kJ/mol rad ²
$\theta_{o\ OCO}$		180.0°

simulations and subsequently were combined with those in Clayff¹⁴ to model the intercalated CO₂ montmorillonite. As noted previously, we rely on the combination rules to evaluate the van der Waals interactions between the CO₂ and the clay surfaces.

Molecular Dynamics Simulations. Results from the molecular dynamics simulations of the CO₂ simulations using the updated force field are, in general, consistent with the thermodynamics and structures of Zhu et al.⁴⁰ We observe no significant difference in the results with the modification of the intramolecular force constants and equilibrium bond length and bond angle. Equilibrium structures from the bulk supercritical CO₂ simulations (310 K and 20 MPa) indicate a bond angle distribution with a mean value of 178° that varies from the linear geometry obtained by Vorholz et al.⁴⁴ for simulations at ambient conditions. The bond bend deformation leads to a net dipole moment for CO₂ at supercritical conditions and which may control the various dimer geometries that have been predicted and observed.⁴⁵

Figure 6 provides snapshots of the equilibrated simulation cells from the molecular dynamics calculations of gas and liquid CO₂. Resulting densities are consistent with the equilibrium coexistence curves for both phases at 300 K as reported by

National Institute of Standards and Technology and Zhu et al.⁴⁰ A snapshot of the equilibrated CO₂–montmorillonite structure shows the distribution of a monolayer of CO₂ molecules arranged along the *ab*-plane of the clay interlayer (Figure 7). Carbon dioxide molecules are oriented subparallel

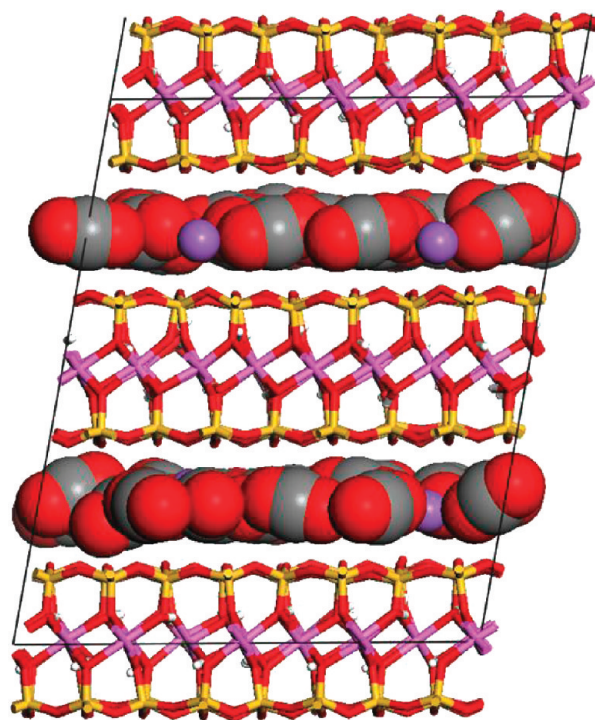


Figure 7. Equilibrated supercell structure of CO₂–montmorillonite model from molecular dynamics simulation using *NPT* ensemble at 310 K and 20 MPa. Projection view is along the *b*-axis.

to the aluminosilicate layers. The mean basal *d*-spacing for the CO₂-intercalated clay is 12.23 Å which is smaller and almost indistinguishable from the 12.35 Å spacing observed for equivalent hydrated clay. We observe on average about four CO₂ molecules coordinated to each of the interlayer sodium ions. The disposition of CO₂ molecules within the clay interlayer from our MD simulations is consistent with recent

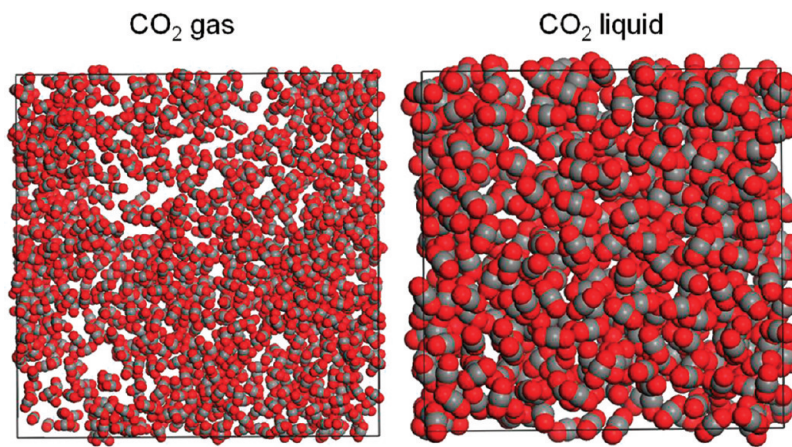


Figure 6. Simulation cells for molecular dynamics simulations of CO₂ as gas with 1408 molecules (left) and liquid with 512 molecules (right). Both simulations were equilibrated at 300 K and 5.6 MPa and represent equilibrium densities associated with subcritical coexistence. A larger simulation cell was required to achieve proper equilibration of the gaseous CO₂ simulation.

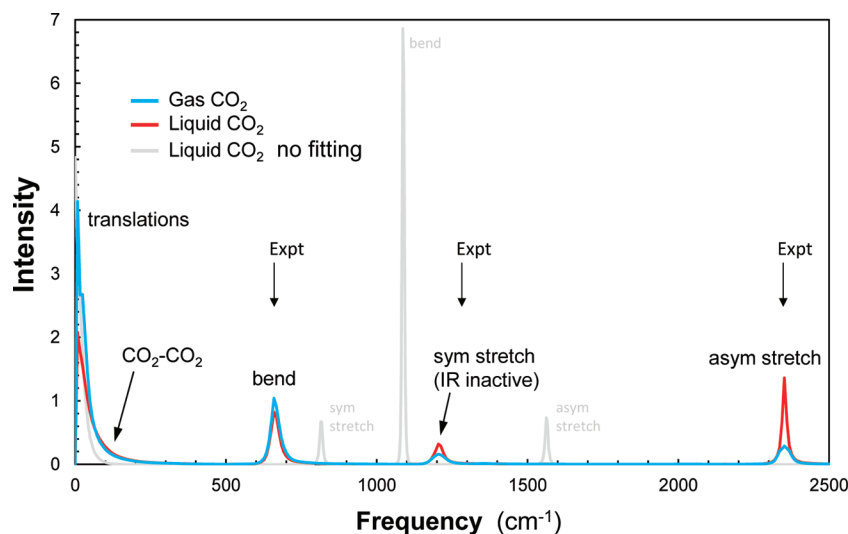


Figure 8. Comparison of power spectra for gas and liquid forms of CO₂ at 300 K and 5.6 MPa based on fitting of stretch and bend force constants to experimental spectra and to a power spectrum (gray) obtained by simulation using force constants derived without fitting.²²

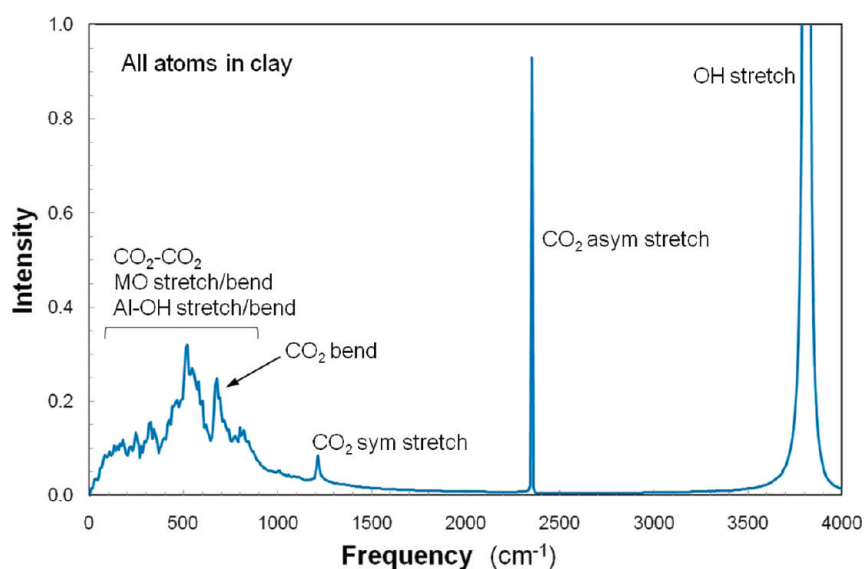


Figure 9. Power spectrum for the CO₂-montmorillonite derived from analysis of all atoms in the molecular dynamics trajectory for NPT ensemble at 310 K and 20 MPa.

Monte Carlo simulations of CO₂ in hydrated Na-montmorillonite²⁵ where H₂O-CO₂ mixtures were investigated.

Power Spectra. Power spectra derived from the molecular dynamics trajectories for the gas and liquid CO₂ simulations are presented in Figure 8 along with a power spectrum derived using an empirical potential that was not optimized for vibrational behavior.²² Carbon dioxide, a linear molecule, is expected to have $3N - 5$ (N is number of atoms) or four vibrational modes. The bending mode is doubly degenerate, so only three peaks are observed in the power spectra. The vibrational frequencies are nearly identical for the gas and liquid phases, and only the intensity significantly varies between the simulations. The asymmetrical stretch mode is the most intense vibrational mode for the liquid, while the bend mode dominates the gas spectrum. The results overall are consistent with observation for gas, liquid, and supercritical phases of CO₂.^{42,46} Experimental infrared spectra of CO₂, including the supercritical phase, also exhibit a Fermi resonance at approximately 1330 cm⁻¹ that incorporates the symmetrical stretch at 1288

cm⁻¹ and the overtone of the bend mode at 667 cm⁻¹.⁴⁶ This resonance, which is a quantum mechanical effect resulting from anharmonicity of the vibrational modes, is not predicted by molecular simulations involving a classical force field model. Of course, no vibrational modes, quantum or classical, would be observed for simulations incorporating a rigid CO₂ model. The low frequencies at less than 100 cm⁻¹ represent molecular translations—diffusion of CO₂ molecules in the simulation cell during the 6 ps window used to evaluate the correlated atomic velocities. The greater intensity observed for the gas phase relative to the liquid is consistent with molecular diffusion and the different densities of the two simulation cells. The low frequency region between 100 and 200 cm⁻¹ is associated with intermolecular associations of CO₂.

Figure 9 provides the power spectrum for the equilibrated CO₂-montmorillonite based on the velocity autocorrelation for all atoms in the simulation. The hydroxyl stretch dominates the spectrum at the highest frequencies and is associated with the hydroxyls coordinated to the octahedral aluminum in the

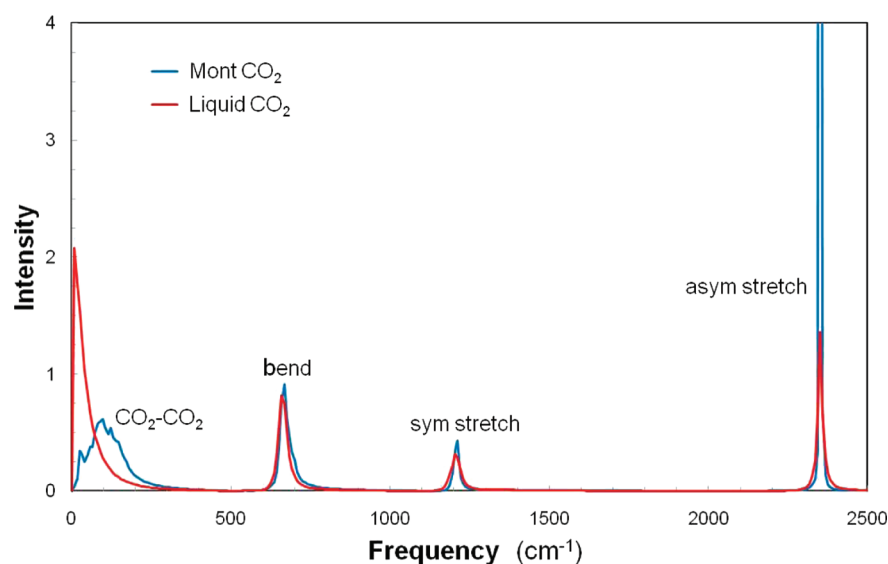


Figure 10. Power spectra for the CO₂ atoms in liquid CO₂ and interlayer CO₂ from the intercalated montmorillonite derived from analysis of the molecular dynamics trajectories for *NPT* ensemble at 310 K and 20 MPa.

montmorillonite layer. The bend mode and two stretch modes for CO₂ are also observed at the same frequencies noted previously. The most intense peak is for the CO₂ asymmetric stretch as observed in simulations of liquid CO₂. Spectral features at the lower frequencies are dominated by metal–oxygen stretch and various oxygen–metal–oxygen bends from tetrahedral silicon and octahedral aluminum. Intermolecular CO₂ interactions probably contribute to some of the intensity along the tail of the translations peak at 100–200 cm⁻¹.

The benefit of using molecular simulations and power spectrum analysis is the ability to separate complex signals and identify specific contributors to the spectrum. This process is best demonstrated in our VACF analysis using only the interlayer CO₂ atoms and removing the clay atoms from the analysis. The Fourier transform of the VACF for the CO₂ component from the CO₂–montmorillonite simulation is presented in Figure 10 along with the power spectrum obtained from the liquid CO₂ simulation as a reference. The power spectrum for the intercalated CO₂, in general, is similar to that for the liquid. The relative intensities are consistent although the asymmetrical stretch mode for the intercalated CO₂ exhibits enhanced intensity, along with a narrowing of the peak, associated with the confinement of the interlayer and direct interaction with two silicate surfaces. The enhanced intensity is probably due to additional induced dipole–ion interactions. The symmetrical stretch for CO₂ occurs at 1210 cm⁻¹ with a slight narrowing and subtle shift to higher frequencies. However, the bend mode for CO₂ at 667 cm⁻¹ is shifted (approximately 10–15 cm⁻¹) to higher frequencies (Figure 11) with intercalation into the montmorillonite. Although it is not clear whether the shift is controlled by the confining space of the interlayer or the association of CO₂ with the interlayer Na⁺, the predicted peak shift appears to be diagnostic of intercalated CO₂. The calculated frequency shift is consistent with diffuse-reflectance FT-IR results³ once proper subtraction of the initial background (KBr prior to CO₂ exposure) is performed (Figure 12). The experimental spectra exhibit a marginal (less than the frequency resolution of the simulation) but consistent blue shift in the bend frequency observed at 668 cm⁻¹. Lastly, the broad peak at low frequency, attributed to intermolecular CO₂

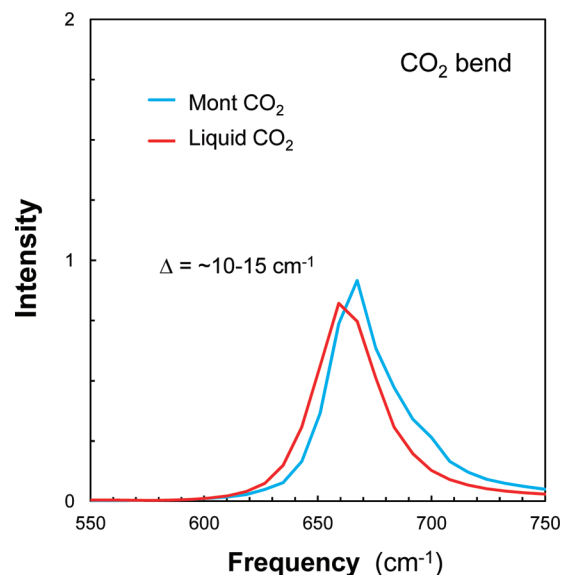


Figure 11. Details of the CO₂ bend mode in the power spectra for the CO₂ atoms in liquid CO₂ and interlayer CO₂ from the intercalated montmorillonite.

interactions, is greatly amplified relative to those librations for liquid CO₂.

To explore power spectra of intercalated CO₂ in the presence of water, two additional intercalated montmorillonite systems were considered. Figure 13 displays basal *d*-spacing change upon increased water content in the interlayer region, and with addition of CO₂ (two molecules per unit cell) at fixed $M_{\text{H}_2\text{O}}/M_{\text{clay}}$. The two systems selected for the power spectra determination are characterized with *d*-spacings observed for equivalent one and two layers of hydrated clay accordingly. The *d*-spacing shifts in the one-layer hydrate from 10.77 ± 0.04 to 12.22 ± 0.03 Å (12% swelling) after CO₂ intercalation, and in the two-layer system the addition of CO₂ results in an expansion to 14.78 ± 0.09 Å from 12.98 ± 0.09 Å. Density profiles of atoms in the interlayer region clearly show separation of CO₂ molecules into two distinct layers similar

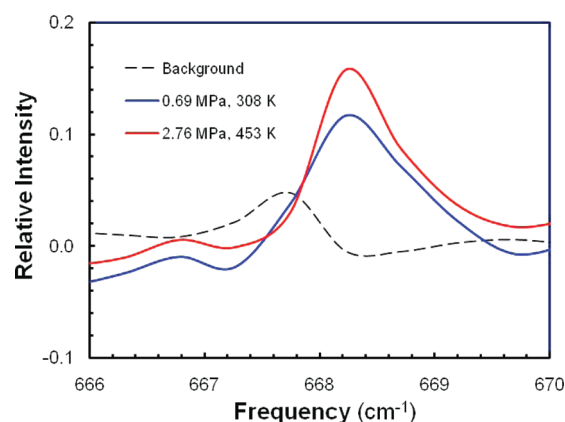


Figure 12. Comparison of the background and residual FT-IR diffuse-reflectance spectra of CO₂-treated montmorillonite (STx-1b), after subtraction of 3x background before exposure to CO₂.

to that observed for a two-layer water network and comparable to the results from Monte Carlo simulations²⁵ of H₂O–CO₂ in a two-layer hydrate of Na–montmorillonite. As it follows from the angle distribution of CO₂ orientation relative to the clay surface, CO₂ molecules experience more free rotational motion in the two-layer system relative to their more constrained behavior in the one-layer system. Regardless, the power spectra for these two examples (not shown) suggest virtually identical vibrational behavior for CO₂ indicating that CO₂ intercalation at different hydrated levels of the montmorillonite may follow a similar mechanism. Power spectra for the intercalated CO₂ computed with water present and with water absent show similar results suggesting that water solvation does not cause a significant shift in the vibrational modes.

Radial Distribution Functions. The use of mixing rules to derive van der Waals energies for H₂O–CO₂ mixtures was recently challenged to improve the quality of MD simulations and the prediction of solubility and transport properties especially at elevated conditions.⁴⁷ Figure 14 provides a

comparison of radial distribution functions derived from atomic trajectories obtained using the flexible CO₂ potentials and the flexible SPC water model used in Clayff with those from the Vleck et al. study based on the EPM2 rigid CO₂ potential²¹ and rigid SPC/E water model but with optimized van der Waals cross-terms for heteroatomic interactions. The simulations used a 6 × 6 × 3 supercell of Na–montmorillonite with the intercalation of a mixture of three water molecules and four CO₂ molecules per unit cell. The radial distribution functions for both potential sets are nearly identical for the association of water molecules to the CO₂ carbon and to the CO₂ oxygen within the clay interlayer. A main peak at 4 Å and a shoulder at 3 Å for the O_{H₂O}–C_{CO₂} distribution function indicate two nearest-neighbor configurations for the molecules, whereas the solitary 3 Å peak for the O_{H₂O}–O_{CO₂} data suggests a relatively uniform distribution of oxygens for either oxygen throughout the interlayer region.

Diffusion Coefficients. One of the key factors for natural clay materials to retain CO₂ in the interlayer region is the diffusion rate of intercalated CO₂. To assess reliability of transport properties for these materials, it is important to compare simulated diffusion of CO₂ with experimental data. However, experimental data for CO₂ diffusion in clay minerals is scarce. Self-diffusion coefficients of pure CO₂ determined by MD simulation at supercritical conditions are reported by Zhu et al.⁴⁰ Their simulations used a similar potential for CO₂ as used in this study and were in excellent agreement with experimental data. Zeebe⁴⁸ used MD to examine the diffusion of rigid CO₂ and other dissolved carbonate species in aqueous solution from 0 to 100 °C. Vleck et al.⁴⁷ derived tracer diffusion coefficients for the H₂O–CO₂ system using a set of polarization-corrected potentials for rigid molecules. Similarly, we have calculated diffusion coefficients for CO₂ in water and compare these results with experimental values.

Table 2 and Figure 15 collect the diffusion coefficients for aqueous CO₂ computed with rigid (both SPC H₂O and CO₂), flexible (both SPC H₂O and CO₂), and flexible (both TIP4P

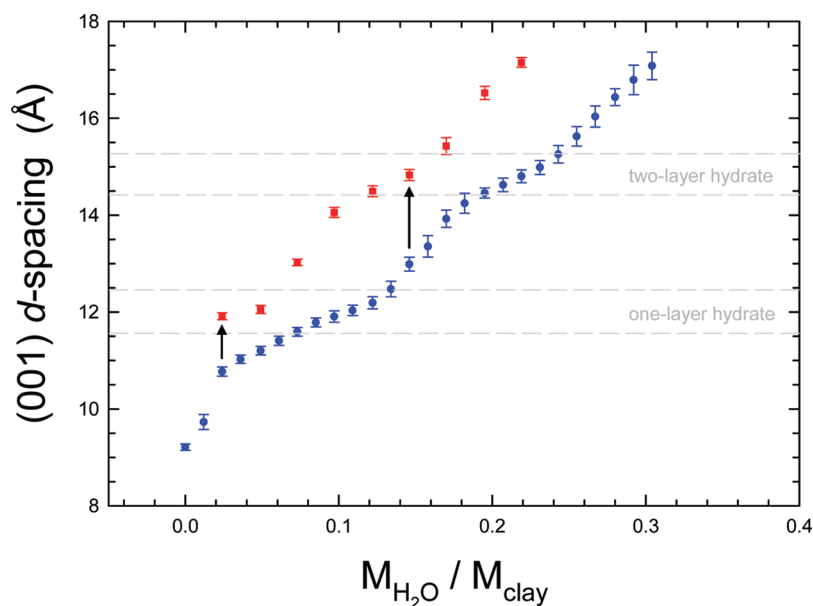


Figure 13. Swelling behavior of Na–montmorillonite upon hydration (blue circles) and after additional intercalation of two molecules of CO₂ per unit cell (red squares) based on *NPT* molecular dynamics simulations at 310 K and 20 MPa. Arrows indicate swelling occurring after CO₂ intercalation in systems with approximately one and six water molecules per unit cell.

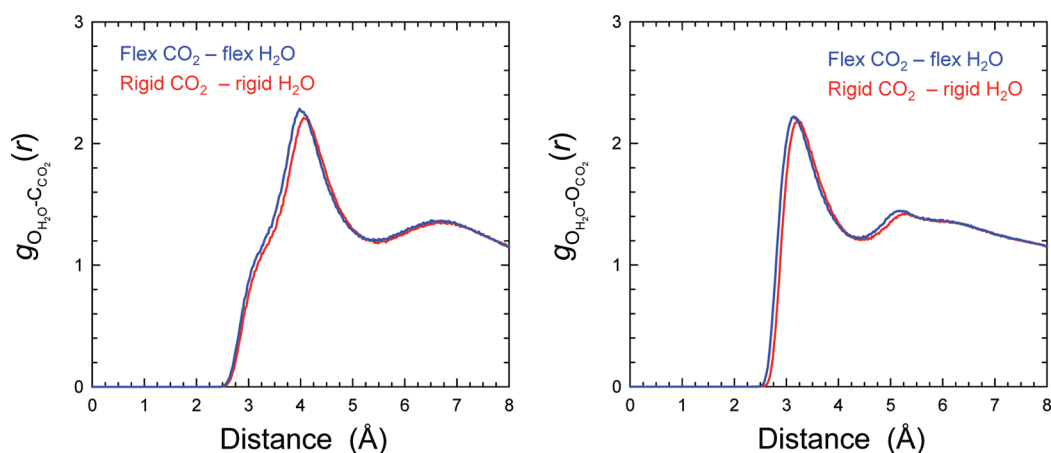


Figure 14. Comparison of the radial distribution functions for $\text{O}_{\text{H}_2\text{O}}-\text{C}_{\text{CO}_2}$ (left) and $\text{O}_{\text{H}_2\text{O}}-\text{O}_{\text{CO}_2}$ (right) pairs from MD simulations of $\text{H}_2\text{O}-\text{CO}_2$ mixtures in intercalated Na-montmorillonite at 348 K and 13 MPa using the flexible CO_2 -flexible SPC (blue) and the rigid EPM2-rigid SPC/E⁴⁷ potentials (red).

Table 2. Diffusion Coefficients of CO_2 in Water (0.1 MPa) Derived from MD Simulations Using Flexible and Rigid Force Fields and from Experiment

temp (K)	D (10^{-9} m ² /s)						
	this study rigid SPC H_2O and CO_2	this study flexible SPC H_2O and CO_2	this study flexible TIP4P H_2O and CO_2	Tamimi et al. ⁴⁹	Himmelblau ⁵⁰	Thomas and Adams ⁵¹	Davidson and Cullen ⁵²
293	2.45 ± 0.22	1.24 ± 0.18	1.26 ± 0.18	1.76	1.60		1.68
303	3.49 ± 0.17	2.10 ± 0.28	2.38 ± 0.23	2.20	2.15		2.25
313	4.65 ± 0.43	2.33 ± 0.29	2.62 ± 0.31	2.93			
323	4.85 ± 0.46	3.40 ± 0.34	3.08 ± 0.17			3.03	
338	5.25 ± 0.38	4.22 ± 0.33	3.92 ± 0.19		4.30	4.40	
348	5.63 ± 0.61	4.69 ± 0.51	6.32 ± 0.31			5.40	
368	9.28 ± 0.83	11.55 ± 1.23	7.58 ± 0.48	8.20			

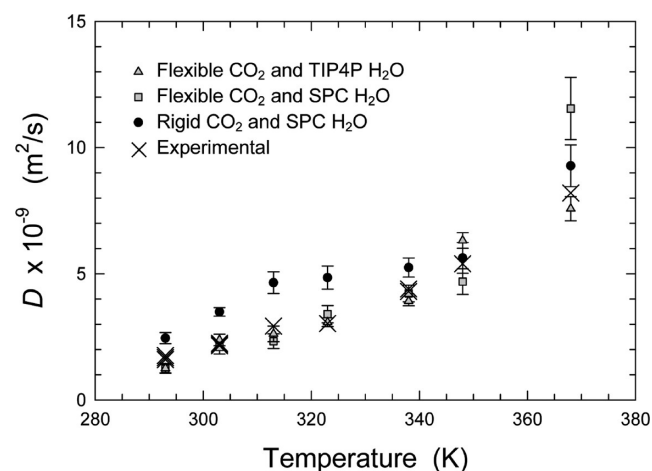


Figure 15. Diffusion coefficients of CO_2 in water obtained by NVT molecular dynamics simulation using flexible and rigid force fields in comparison with experimental data.

H_2O and CO_2) force fields together with experimental data. Using the rigid potentials leads to overestimation of the diffusion coefficients, while combinations of the flexible interatomic potentials provide considerable agreement with experimental values. Thus, the flexible force field of CO_2 developed in this work delivers a superior performance over the potential using the rigid geometry. Because Clayff was optimized with a flexible SPC water force field, one can expect to retrieve reliable diffusivities of CO_2 in the interlayer region of

clay minerals either under supercritical conditions or in a liquid water phase. Figure 16 presents an Arrhenius plot of CO_2 diffusion coefficients derived from the flexible-based potentials in comparison with experimental data. Arrhenius activation energies and pre-exponential values derived from the best fits of the data are presented in Table 3. Diffusion results for the temperature range are in relatively good agreement and consistent with literature values.⁴⁹

Quantum Simulations. We used electronic structure calculations to derive optimized configurations of isolated CO_2 and Na^+-CO_2 clusters. Optimized structures using the Gaussian 03 software package²⁷ were obtained at the B3LYP/Aug-cc-pVDZ and MP2/Aug-cc-pVDZ levels of theory and subsequently used for normal-mode analysis to derive vibrational intensities and frequencies. A linear configuration of the CO_2 molecule with Na^+ is observed for the optimized structures using both methods. The electrostatics controls the strong interaction of the cation with either of the terminal oxygen atoms. The normal-mode results for the optimized clusters (Table 4) indicate a shift to lower frequencies for all modes using the MP2 methods relative to those obtained using the B3LYP functionals. In both methods, we observe a blue shift of about 40 cm^{-1} in the asymmetrical stretch frequency of CO_2 to approximately 2420 cm^{-1} when the molecule is associated with Na^+ . Similarly, there is a blue shift of approximately 15 cm^{-1} for the symmetrical stretch. In contrast, the experimental FT-IR spectrum of Na-montmorillonite with intercalated CO_2 suggests a small red shift (5 cm^{-1}) of the asymmetric CO_2 stretch. This different observation suggests

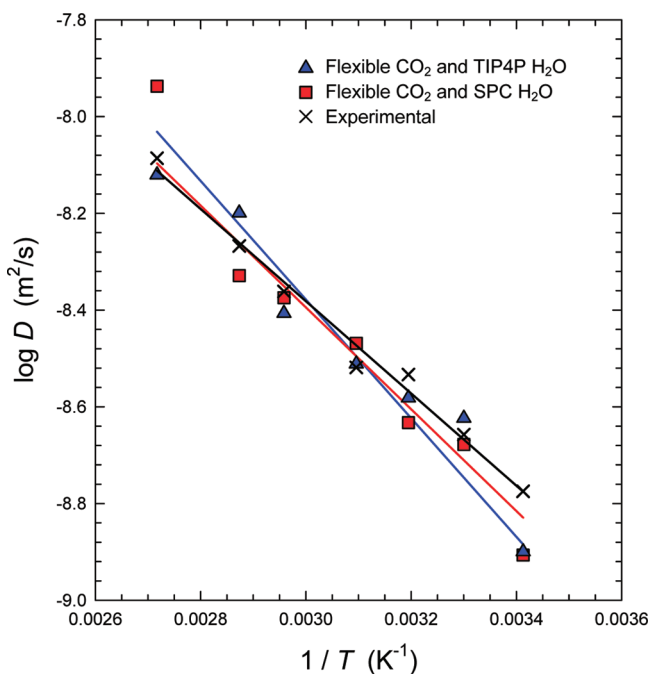


Figure 16. Arrhenius plots for diffusion of CO₂ in water. Linear fits were made for experimental data and results from *NVT* molecular dynamics simulations using flexible CO₂ with flexible TIP4P H₂O force fields and flexible CO₂ with flexible SPC H₂O combination. *R*² values for the fits are above 0.97.

Table 3. Arrhenius Activation Energy and Pre-exponential Term for Diffusion of CO₂ in Water Obtained from MD Simulation and from Experiment

	<i>E</i> _a (kcal/mol)	<i>D</i> ₀ (10 ⁻⁶ , m ² /s)
experiment	4.28 ± 0.12	2.69 ± 0.34
flex CO ₂ with flex TIP4P	4.83 ± 0.27	5.81 ± 0.73
flex CO ₂ with flex SPC	5.51 ± 0.32	20.1 ± 4.4

that the confinement environment of the hydrated clay phase could be responsible for the peak shift. The MD simulations of the Na–montmorillonite–CO₂ system predict virtually no dependency of the asymmetric stretch mode upon intercalation,

somewhat comparable to the experimental observation. In this regard, the blue shift of the bending mode of CO₂ predicted using the MD simulations can also be associated with the confinement environment of the interlayer region. We observe in the cluster calculations that the interaction with Na⁺ alone leads to the opposite trend. To account for the influence of the clay phase, we plan to use *ab initio* MD approach to probe the response of the asymmetrical CO₂ mode to evaluate the different chemical environments.

CONCLUSIONS

We have completed a series of molecular dynamics simulations to better assess the molecular interactions associated with incorporation of CO₂ in the interlayer of montmorillonite clay and to simulate vibrational spectra to help validate the models with experimental observation. We first extended several published three-site potential models of CO₂ to derive a set of accurate interaction parameters that are compatible with the widely used Clayff force field. The extended set of interaction parameters permits full flexibility of the molecule with bond stretching and bond angle bending. Comparison of experimental and theoretical data with our molecular dynamics simulations of gas and liquid CO₂ confirms the accuracy of the new force field. Also, a comparison of diffusion coefficients of CO₂ in water derived from molecular dynamics simulations demonstrates the accuracy of using flexible force field models for CO₂ and H₂O. Based on the experimental evidence for CO₂ intercalation in montmorillonite clay, we developed a conceptual model for the intercalated structure and performed a series of molecular dynamics simulations. Power spectra were derived from the equilibrated atomic and velocity trajectories that allowed the isolation of signal from key components of the molecular model. Normal-mode analysis of optimized structures of CO₂ and Na–CO₂ derived from density functional calculations are in general agreement with the classical models although the trends in vibrational frequencies are inconsistent with experiment and MD simulations of the Na⁺–montmorillonite–CO₂ system, suggesting that the confinement environment plays a dominant role in the direction of frequency shifts. Power spectra analyses of the molecular dynamics trajectories indicate the bending motion of CO₂ at approximately 667 cm⁻¹ is blue-shifted by 10–15 cm⁻¹

Table 4. Normal Mode Analysis of Quantum-Derived CO₂ Cluster Models

method	O=C=O ^a			Na ⁺ ...O=C=O		
	symmetry	IR intensity	frequency cm ⁻¹	symmetry	IR intensity	frequency cm ⁻¹
B3LYP/ aug-cc-pVDZ	Σ _u	656.54	2388.58	Σ	696.94	2423.42
	Σ _g	0	1354.38	Σ	25.83	1367.75
	Π _u	28.75	667.52	Π	33.81	653.05
	Π _u	28.75	667.52	Π	33.81	653.05
MP2/ aug-cc-pVDZ				Σ	43.47	220.65
				Π	7.44	76.19
				Π	7.44	76.19
	Σ _u	567.61	2379.38	Σ	428.55	2420.59
	Σ _g	0	1305.47	Σ	14.14	1320.70
	Π _u	21.46	655.45	Π	26.14	641.97
	Π _u	21.46	655.45	Π	26.14	641.97
			Σ	68.85	204.35	
			Π	7.76	65.16	
			Π	7.76	65.16	

^aExperimental fundamentals of CO₂ are at 667, 1333, and 2349 cm⁻¹.⁴³

when CO₂ is in the clay interlayer. The asymmetric stretch of CO₂ at 2349 cm⁻¹ is virtually unaffected by the environment of the clay and occurs at the same frequency as that for liquid CO₂. This result is similar to experimental findings from diffuse-reflectance infrared spectroscopy showing that the asymmetrical stretch mode is almost unaffected after exposure of Ca–montmorillonite and Na–montmorillonite to gaseous CO₂. In contrast, the blue shift in the CO₂ bending mode with intercalation determined by molecular simulation is observed in the experimental spectrum after careful subtraction of background. The appearance of additional red-shifted peaks in experimental spectra, which become dominant after exposure of the clays to supercritical CO₂, is not explained in this study and could be attributed to the unaccounted molecular configurations having stronger binding interactions involving intercalated CO₂ molecules. This computational chemistry investigation provides a proof of concept that molecular simulation methods can provide important insights into possible molecular mechanisms associated with CO₂ capture in complex natural materials.

AUTHOR INFORMATION

Corresponding Author

*Telephone: 505-844-7216. Fax: 505-844-7354. E-mail: rtcygan@sandia.gov.

Notes

The authors declare no competing financial interest.

ACKNOWLEDGMENTS

This work was funded in part by the Sandia National Laboratories Laboratory Directed Research and Development Program. E.M.M performed this work under contract DE-FE000-4000, Subtask 4000.4.600.251.001 in support of the National Energy Technology Laboratory's Office of Research and Development. The authors are appreciative of the support of John Merson and Mark Rigali at Sandia National Laboratories and George Guthrie at National Energy Technology Laboratory to help expand fundamental research on carbon capture using clay materials. Development of the flexible force field is based upon work supported as part of the Center for Frontiers of Subsurface Energy Security, an Energy Frontier Research Center funded by the U.S. Department of Energy, Office of Science, Office of Basic Energy Sciences under Award Number DE-SC-0001114. Sandia National Laboratories is a multiprogram laboratory operated by Sandia Corporation, a wholly owned subsidiary of Lockheed Martin Corporation, for the U.S. Department of Energy's National Nuclear Security Administration under Contract DE-AC04-94AL85000. This article was prepared as an account of work sponsored by an agency of the U.S. Government. Neither the U.S. Government nor any agency thereof, nor any of their employees, makes any warranty, express or implied, or assumes any legal liability or responsibility for the accuracy, completeness, or usefulness of any information, apparatus, product, or process disclosed, or represents that its use would not infringe privately owned rights. Reference herein to any specific commercial product, process, or service by trade name, trademark, manufacturer, or otherwise does not necessarily constitute or imply its endorsement, recommendation, or favoring by the U.S. Government or any agency thereof. The views and opinions of authors expressed herein do not

necessarily state or reflect those of the U.S. Government or any agency thereof.

REFERENCES

- (1) Busch, A.; Alles, S.; Gensterblum, Y.; Prinz, D.; Dewhurst, D. N.; Raven, M. D.; Stanjek, H.; Krooss, B. M. *Int. J. Greenhouse Gas Control* **2008**, *2*, 297–308.
- (2) Romanov, V. N.; Ackman, T. E.; Soong, Y.; Kleinman, R. L. *Environ. Sci. Technol.* **2009**, *43*, 561–564.
- (3) Romanov, V. N.; Howard, B. H.; Lynn, R. J.; Warzinski, R. P.; Hur, T. B.; Myshakin, E. M.; Lopano, C. L.; Voora, V. K.; Al-Saidi, W. A.; Jordan, K. D.; Cygan, R. T.; Guthrie, G. D. *CO₂ Interaction with Geomaterials*; American Geophysical Union: San Francisco, CA, 2010; H11J01.
- (4) Bacsik, Z.; Atluri, R.; Garcia-Bennett, A. E.; Hedin, N. *Langmuir* **2010**, *26*, 10013–10024.
- (5) Favre, E.; Bounaceur, R.; Roizard, D. *J. Membr. Sci.* **2009**, *328*, 11–14.
- (6) Zhao, G. Y.; Aziz, B.; Hedin, N. *Appl. Energy* **2010**, *87*, 2907–2913.
- (7) Wang, Y.; Bryan, C.; Xu, H.; Gao, H. *Geology* **2003**, *31*, 387–390.
- (8) Benson, S. M.; Cole, D. R. *Elements* **2008**, *4*, 325–331.
- (9) Kharaka, Y. K.; Cole, D. R. Geochemistry of geologic sequestration of carbon dioxide. In *Frontiers in Geochemistry: Contribution of Geochemistry to the Study of the Earth*; Harmon, R. S., Parker, A., Eds.; Blackwell Publishing: Chichester, West Sussex, U.K., 2011.
- (10) Boyd, S. A.; Sheng, G. Y.; Teppen, B. J.; Johnston, C. J. *Environ. Sci. Technol.* **2001**, *35*, 4227–4234.
- (11) Gu, C.; Liu, C.; Johnston, C. T.; Teppen, B. J.; Li, H.; Boyd, S. A. *Environ. Sci. Technol.* **2011**, *45*, 1399–1406.
- (12) Tzavalas, S.; Gregoriou, V. G. *Vib. Spectrosc.* **2009**, *51*, 39–43.
- (13) Wang, L.; Zhang, M.; Redfern, S. A. T. *Clays Clay Miner.* **2003**, *51*, 439–444.
- (14) Cygan, R. T.; Liang, J.-J.; Kalinichev, A. G. *J. Phys. Chem. B* **2004**, *108*, 1255–1266.
- (15) Ockwig, N. W.; Greathouse, J. A.; Durkin, J. S.; Cygan, R. T.; Daemen, L. L.; Nenoff, T. M. *J. Am. Chem. Soc.* **2009**, *131*, 8155–8162.
- (16) Smith, D. E.; Wang, Y.; Chaturvedi, A.; Whitley, H. D. *J. Phys. Chem. B* **2006**, *110*, 20046–20054.
- (17) Fu, M. H.; Zhang, Z. Z.; Low, P. F. *Clays Clay Miner.* **1990**, *38*, 485–492.
- (18) Cygan, R. T.; Greathouse, J. A.; Heinz, H.; Kalinichev, A. G. *J. Mater. Chem.* **2009**, *19*, 2470–2481.
- (19) Thyveetil, M. A.; Coveney, P. V.; Greenwell, H. C.; Suter, J. L. *J. Am. Chem. Soc.* **2008**, *130*, 4742–4756.
- (20) Accelrys. *Materials Studio*, Release 5.5 ed.; Accelrys Software Inc.: San Diego, CA, 2010.
- (21) Harris, J. G.; Yung, K. H. *J. Phys. Chem.* **1995**, *99*, 12021–12024.
- (22) Qin, Y.; Yang, X. N.; Zhu, Y. F.; Ping, J. L. *J. Phys. Chem. C* **2008**, *112*, 12815–12824.
- (23) Nosé, S. *Mol. Phys.* **1984**, *52*, 255–268.
- (24) Berendsen, H. J. C.; Postma, J. P. M.; Vangunsteren, W. F.; Dinola, A.; Haak, J. R. *J. Chem. Phys.* **1984**, *81*, 3684–3690.
- (25) Botan, A.; Rotenberg, B.; Marry, V.; Turq, P.; Noetinger, B. *J. Phys. Chem. C* **2010**, *114*, 14962–14969.
- (26) Allen, M. P.; Tildesley, D. J. *Computer Simulation of Liquids*; Oxford University Press: Oxford, U.K., 1987.
- (27) Frisch, M. J.; Trucks, G. W.; Schlegel, H. B.; Scuseria, G. E.; Robb, M. A.; Cheeseman, J. R.; Montgomery, J. A.; Vreven, T.; Kudin, K. N.; Burant, J. C.; Millam, J. M.; Iyengar, S. S.; Tomasi, J.; Barone, V.; Mennucci, B.; Cossi, M.; Scalmani, G.; Rega, N.; Petersson, G. A.; Nakatsuji, H.; Hada, M.; Ehara, M.; Toyota, K.; Fukuda, R.; Hasegawa, J.; Ishida, M.; Nakajima, T.; Honda, Y.; Kitao, O.; Nakai, H.; Klene, M.; Li, X.; Knox, J. E.; Hratchian, H. P.; Cross, J. B.; Bakken, V.; Adamo, C.; Jaramillo, J.; Gomperts, R.; Stratmann, R. E.; Yazyev, O.; Austin, A. J.; Cammi, R.; Pomelli, C.; Ochterski, J. W.; Ayala, P. Y.; Morokuma, K.; Voth, G. A.; Salvador, P.; Dannenberg, J. J.; Zakrzewski, V. G.; Dapprich, S.; Daniels, A. D.; Strain, M. C.;

Farkas, O.; Malick, D. K.; Rabuck, A. D.; Raghavachari, K.; Foresman, J. B.; Ortiz, J. V.; Cui, Q.; Baboul, A. G.; Clifford, S.; Cioslowski, J.; Stefanov, B. B.; Liu, G.; Liashenko, A.; Piskorz, P.; Komaromi, I.; Martin, R. L.; Fox, D. J.; Keith, T.; Al-Laham, M. A.; Peng, C. Y.; Nanayakkara, A.; Challacombe, M.; Gill, P. M. W.; Johnson, B.; Chen, W.; Wong, M. W.; Gonzalez, C.; Pople, J. A. *Gaussian 03*; Gaussian, Inc.: Wallingford, CT, 2003.

- (28) Becke, A. D. *J. Chem. Phys.* **1993**, *98*, 5648–5652.
- (29) Vosko, S. H.; Wilk, L.; Nusair, M. *Can. J. Phys.* **1980**, *58*, 1200–1211.
- (30) Lee, C. T.; Yang, W. T.; Parr, R. G. *Phys. Rev. B* **1988**, *37*, 785–789.
- (31) Møller, C.; Plesset, M. S. *Phys. Rev.* **1934**, *46*, 618–622.
- (32) Frisch, M. J.; Headgordon, M.; Pople, J. A. *Chem. Phys. Lett.* **1990**, *166*, 275–280.
- (33) Frisch, M. J.; Headgordon, M.; Pople, J. A. *Chem. Phys. Lett.* **1990**, *166*, 281–289.
- (34) Foresman, J. B.; Frisch, A. *Exploring Chemistry with Electronic Structure Methods: A Guide to Using Gaussian*, second ed.; Gaussian, Inc.: Pittsburgh, PA, 1996.
- (35) Raabe, G.; Sadus, R. J. *J. Chem. Phys.* **2011**, *134*.
- (36) Nieto-Draghi, C.; de Bruin, T.; Perez-Pellitero, J.; Avalos, J. B.; Mackie, A. D. *J. Chem. Phys.* **2007**, *126*, 064509.
- (37) Zhang, Z. G.; Duan, Z. H. *J. Chem. Phys.* **2005**, *122*, 214507.
- (38) Murthy, C. S.; Singer, K.; McDonald, I. R. *Mol. Phys.* **1981**, *44*, 135–143.
- (39) Halgren, T. A. *J. Am. Chem. Soc.* **1992**, *114*, 7827–7843.
- (40) Zhu, A. M.; Zhang, X. B.; Liu, Q. L.; Zhang, Q. G. *Chin. J. Chem. Eng.* **2009**, *17*, 268–272.
- (41) Liang, J. Y.; Lipscomb, W. N. *Proc. Natl. Acad. Sci. U.S.A.* **1990**, *87*, 3675–3679.
- (42) Günzler, H.; Gremlich, H. *IR Spectroscopy: An Introduction*; Wiley-VCH: New York, 2002.
- (43) Shimanouchi, T. Molecular vibrational frequencies. In *NIST Chemistry WebBook, NIST Standard Reference Database*, 69 ed.; Linstrom, P. J., Mallard, W. G., Eds.; National Institute of Standards and Technology: Gaithersburg, MD, 2001.
- (44) Vorholz, J.; Harismiadis, V. I.; Rumpf, B.; Panagiotopoulos, A. Z.; Maurer, G. *Fluid Phase Equilib.* **2000**, *170*, 203–234.
- (45) Cabaço, M. I.; Longelin, S.; Danten, Y.; Besnard, M. *J. Chem. Phys.* **2008**, *128*, 074507.
- (46) Yagi, Y.; Tsugane, H.; Inomata, H.; Saito, S. *J. Supercrit. Fluids* **1993**, *6*, 139–142.
- (47) Vlcek, L.; Chialvo, A. A.; Cole, D. R. *J. Phys. Chem. B* **2011**, *115*, 8775–8784.
- (48) Zeebe, R. E. *Geochim. Cosmochim. Acta* **2011**, *75*, 2483–2499.
- (49) Tamimi, A.; Rinker, E. B.; Sandall, O. C. *J. Chem. Eng. Data* **1994**, *39*, 330–332.
- (50) Himmelblau, D. M. *Chem. Rev.* **1964**, *64*, 527–550.
- (51) Thomas, W. J.; Adams, M. J. *Trans. Faraday Soc.* **1965**, *61*, 668–673.
- (52) Davidson, J. F.; Cullen, E. J. *Trans. Inst. Chem. Eng.* **1957**, *35*, 51–60.